Experimental Implementation of Retrospective Cost Adaptive Control for Suppressing Thermoacoustic Oscillations in a Rijke Tube

Juan A. Paredes and Dennis S. Bernstein, *Life Fellow, IEEE*

***Abstract*— Thermoacoustic systems are self-oscillating due to the fact that a constant input (e.g., fuel rate in gas-turbine combustors) yields an asymptotically oscillatory response. This behavior arises from the interaction between combustion and acoustics, resulting in thermoacoustic oscillations. Under varying operating conditions, the dynamics of thermoacoustic systems may change dramatically, which may require that active suppression controllers can be tuned for specific working conditions. This work provides an experimental investigation of retrospective cost adaptive control for suppressing thermoacoustic oscillations under sampled-data control and varying system operating conditions. This approach is first applied to a Rijke-tube emulation model for hyperparameter selection and subsequently to an experimental Rijke-tube setup. Physical experiments are conducted to investigate the performance and robustness of the adaptive controller under varying operating conditions.**

***Index Terms*— Active control, adaptive control, Rijke tube, self-excited systems (SESs), suppression, thermoacoustic oscillations.**

I. Introduction

A SELF-EXCITED system (SES) has the property that, for all constant inputs, the response is asymptotically oscillatory. These oscillations arise from a combination of destabilizing and stabilizing effects. Roughly speaking, destabilization causes the response to grow from the vicinity of an equilibrium, whereas, far from the equilibrium, the effective feedback gain decreases, leading to oscillations [1]. A typical control objective for SES is thus suppression of the oscillations. Although a Lyapunov-stable linear system with nonzero poles on the imaginary axis or time delays may have an oscillatory response, such a system is not robustly self-excited; consequently, a realistic SES model is necessarily nonlinear.

SESs arise in a vast range of applications, including biochemical systems, aeroelasticity, and combustion [2], [3], [4], [5], [6], [7], [8], [9], [10], [11]. As in the case of a wind turbine, whose blades spin in response to the ambient wind flow, self-excited dynamics can be extremely useful. In other cases, however, SES dynamics may be undesirable, as demonstrated by the destruction of the Tacoma-Narrows bridge, which was due to trailing vortices rather than resonant modes [12]. In addition to their practical applications, SES systems provide motivation for developing new techniques for modeling and control [13], [14], [15], [16], [17], [18].

A widely studied SES is the Rijke tube, which consists of a cylinder and a heating element. A Rijke tube is a spatially 1-D thermoacoustic system that is highly susceptible to thermoacoustic oscillation. Under constant heating, the Rijke tube undergoes self-excited oscillations due to the interaction between the heat source and fluid dynamics. The physics of the Rijke tube has been extensively analyzed, with the original work by Rijke [19] and subsequent work of Rayleigh [20]. In particular, Rayleigh showed that, under certain conditions involving heat and geometry, thermoacoustic oscillations arise from the feedback interaction of the expansion and compression of the air and the heat flux. In thermoacoustic oscillations, the positive feedback between the acoustic field of the system and the unsteady rate of heat release from combustion creates pressure waves whose amplitude increases until it is limited by nonlinear effects. Self-excited pressure oscillations can cause structural vibrations within a combustor, which results in premature component wear and thus reduced lifespan of the combustor, reduced efficiency, and possible system failure [21], [22], [23] [24, pp. 3–26].

A Rijke tube provides an ideal venue for developing and implementing modeling and control techniques for SES. In particular, a laboratory-scale Rijke tube requires only a suitable tube and heating element; for feedback control, a microphone and speaker provide high-authority, high-bandwidth sensing and actuation. All of these components are inexpensive and accessible to classroom demonstrations. Most importantly, control experiments involving a Rijke tube are safe to run since no damage is incurred when the feedback controller inadvertently amplifies the thermoacoustic oscillations. The most expensive component needed for digital feedback control is the processor for controller implementation. For the adaptive control experiments reported in the present work, we use a dSpace Scalexio system; low-power embedded processors are sufficient, however, for implementing fixed-gain control laws.

Extensive research has been devoted to modeling thermoacoustic oscillations [1], [25], [26], [27], [28], [29], [30],

Manuscript received 9 November 2022; revised 11 November 2022, 15 November 2022, and 7 February 2023; accepted 17 March 2023. Date of publication 4 April 2023; date of current version 23 October 2023. This work was supported in part by the NSF under Grant CMMI 1634709. Recommended by Associate Editor J. T. Gravdahl. *(Corresponding author: Juan A. Paredes.)*

The authors are with the Aerospace Engineering Department, University of Michigan, Ann Arbor, MI 48109 USA (e-mail: jparedes@umich.edu; dsbaero@umich.edu).

Color versions of one or more figures in this article are available at https://doi.org/10.1109/TCST.2023.3262223.

Digital Object Identifier 10.1109/TCST.2023.3262223

[31] and suppressing these instabilities using a wide variety of techniques [13], [32], [33]. Experimental applications of various control algorithms are reported; in particular, Heckl [34], Zalluhoglu et al. [35], and de Andrade [36] implemented phase shift controllers, Kemal and Bowman [37] implemented a least-mean-squares (LMS) controller, Annaswamy et al. [38] implemented linear-quadratic-Gaussian (LQG) and H_∞ controllers, Morgans and Annaswamy [39] implemented self-tuning regulators, Vaudrey et al. [40] implemented a time-averaged gradient controller, Illingworth and Morgans [41] implemented an LQG controller and a Nussbaum adaptive controller, Wei et al. [42] implemented an adaptive controller based on dynamic compensation, Blonbou et al. [43] implemented a neural-network controller, and de Andrade et al. [44] proposed a backstepping-based controller. An interesting aspect of these control studies is the fact that, although a Rijke tube is an SES and thus is nonlinear, all of the techniques applied to the Rijke tube in [1], [34], [35], [36], [38], and [41] are based on linear models and methodologies. These results show that linear controllers are effective for this nonlinear system. Furthermore, as mentioned in [13], while model-based controllers may suffer loss of performance due to uncertainty or changes in operating conditions, adaptive controllers can achieve suppression over a wide range of operating conditions. However, model-based controllers require detailed modeling information about the system in order to achieve closed-loop stability and robustness. To reduce the need for modeling, a data-driven, adaptive controller that requires minimal modeling information is desirable.

The goal of this work is to experimentally investigate the modeling requirements, performance, and robustness of retrospective cost adaptive control (RCAC) [45], [46] for suppressing thermoacoustic oscillations in a Rijke tube. The focus of this work is on the experimental application of data-driven control. The stability analysis for RCAC is discussed in [47]; however, within the current experimental data-driven context, no theoretical truth model is available. This present article is a major expansion of the preliminary results presented in [48]. In particular, this work provides a more complete discussion of the methodology, as well as substantially more extensive experimental results.

A crucial aspect of the adaptive controller is the selection of hyperparameters, which determine the speed of adaptation, the assumed modeling information, and the controller order. A hyperparameter selection procedure based on closed-loop numerical simulation is shown in Fig. 1. First, physical Rijke-tube experiments are conducted in an open-loop configuration (no feedback control) to obtain pressure measurements. Then, a fit procedure is applied, where the parameters of the Rijke-tube model are chosen to capture the frequency and magnitude of the highest peak of the open-loop pressure measurements. This procedure yields an emulation model, which is used for adaptive closed-loop numerical simulations to select hyperparameters based on achieved oscillation suppression. The selected hyperparameters are then used in physical closed-loop Rijke-tube experiments. For these experiments, the adaptive controller is implemented on a dSpace Scalexio system to suppress thermoacoustic oscillations generated by the coil

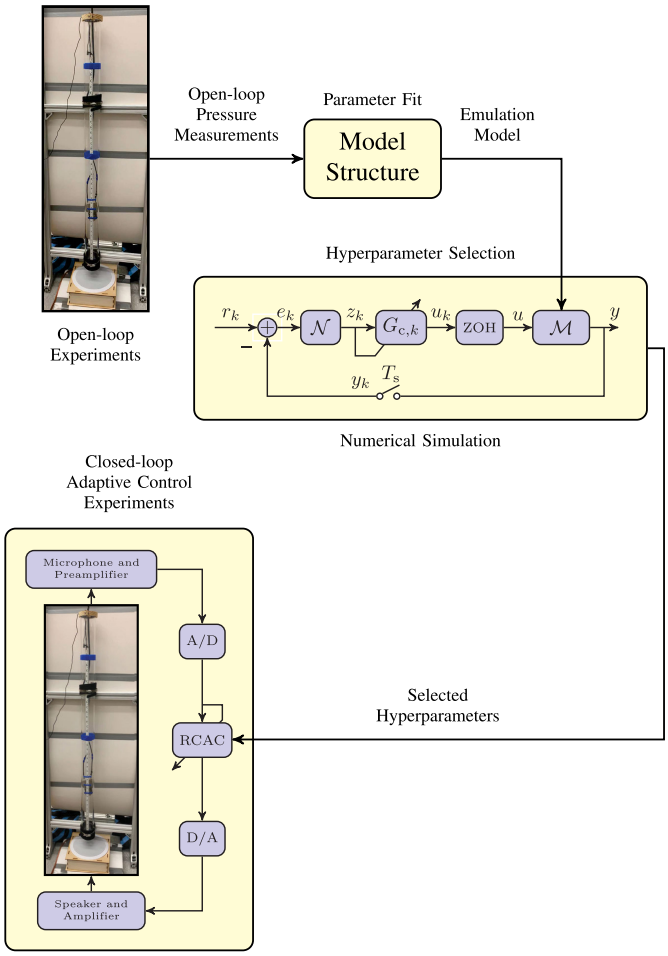

Fig. 1. Hyperparameter selection procedure. The objective is to select initial hyperparameters by applying the adaptive controller to an emulation model of the experimental Rijke-tube setup.

heat for various coil positions and voltage levels. Note that the emulation model is used only to select hyperparameters for adaptation and is otherwise not used or needed for feedback control.

The main goal of these experiments is to examine the properties of the controller under various experimental scenarios, including the effect of modified hyperparameters on the time it takes for the adaptive controller to suppress oscillations, the performance and robustness of the frozen-gain adaptive controller, the ability of the adaptive controller to readapt under changes in working conditions, the stability of the adaptive controller under changes in its gain, and the effect of the relative degree of the closed-loop target model on the level of suppression. The experimental scenarios are designed to test the robustness of the adaptive controller under off-nominal perturbations that reflect real-world conditions. The level of suppression of the thermoacoustic oscillations, referred to as oscillation suppression, is used to evaluate the performance of the controller, which is defined to be the ratio of the steady-state open-loop maximum time-domain pressure amplitude to the steady-state closed-loop maximum time-domain pressure amplitude in dB.

The contents of this article are given as follows. Section II describes the adaptive control law considered in this article for adaptive suppression. Section III considers the approach

under which the discrete-time adaptive controller interacts with continuous-time systems. Section IV presents the experimental Rijke-tube setup. Section V presents a Rijke-tube model. Section VI presents the parameters used in the Rijke-tube model given in Section V to obtain the Rijke-tube emulation model. To determine the initial hyperparameters, Section VII presents numerical examples where the adaptive controller suppresses the emulation model of the Rijke tube. Section VIII presents the physical closed-loop Rijke-tube experiments. Finally, Section IX presents the conclusions.

II. Retrospective Cost Adaptive Control

Consider the strictly proper, discrete-time, input–output controller

$$u_k = \sum_{i=1}^{l_c} P_{i,k} u_{k-i} + \sum_{i=1}^{l_c} Q_{i,k} z_{k-i} \tag{1}$$

where $u_k \in \mathbb{R}^{l_u}$ is the controller output and thus the control input, $z_k \in \mathbb{R}^{l_z}$ is the measured performance variable, l_c is the controller-window length, and, for all $i \in \{1, \ldots, l_c\}$, $P_{i,k} \in \mathbb{R}^{l_u \times l_u}$ and $Q_{i,k} \in \mathbb{R}^{l_u \times l_z}$ are the controller coefficient matrices. The controller (1) can be written as

$$u_k = \phi_k \theta_k \tag{2}$$

where

$$\phi_k \triangleq \begin{bmatrix} u_{k-1}^{\mathsf{T}} & \cdots & u_{k-l_c}^{\mathsf{T}} & z_{k-1}^{\mathsf{T}} & \cdots & z_{k-l_c}^{\mathsf{T}} \end{bmatrix} \otimes I_{l_u} \in \mathbb{R}^{l_u \times l_\theta} \tag{3}$$

$$\theta_k \triangleq \operatorname{vec}\begin{bmatrix} P_{1,k} & \cdots & P_{l_c,k} & Q_{1,k} & \cdots & Q_{l_c,k} \end{bmatrix} \in \mathbb{R}^{l_\theta} \tag{4}$$

$l_\theta \triangleq l_c l_u (l_u + l_z)$, and θ_k is the vector of controller coefficients, which are updated at each time step k. If z_k and u_k are scalar, then the single-in, single-out (SISO) transfer function of (1) from z_k to u_k is given by

$$G_{c,k}(\mathbf{q}) = \frac{Q_{1,k}\mathbf{q}^{l_c-1} + \cdots + Q_{l_c,k}}{\mathbf{q}^{l_c} - P_{1,k}\mathbf{q}^{l_c-1} - \cdots - P_{l_c,k}} \tag{5}$$

where $\mathbf{q}$ is the forward-shift operator.

Next, define the retrospective cost variable

$$\hat{z}_k(\hat{\theta}) \triangleq z_k - G_f(\mathbf{q})\big(u_k - \phi_k \hat{\theta}\big) \tag{6}$$

where G_f is an $l_z \times l_u$ asymptotically stable, strictly proper transfer function, and $\hat{\theta} \in \mathbb{R}^{l_\theta}$ is the controller coefficient vector determined by optimization in the following. The rationale underlying (6) is to replace the applied past control inputs with the reoptimized control input $\phi_k \hat{\theta}$ so that the closed-loop transfer function from $u_k - \phi_k \theta_{k+1}$ to z_k matches G_f [45], [46]. Consequently, G_f serves as a closed-loop target model for adaptation.

In this present article, G_f is chosen to be a finite-impulse-response transfer function of window length l_f of the form

$$G_f(\mathbf{q}) \triangleq \sum_{i=1}^{l_f} N_i \mathbf{q}^{-i} \tag{7}$$

where $N_1, \ldots, N_{l_f} \in \mathbb{R}^{l_z \times l_u}$. We can thus rewrite (6) as

$$\hat{z}_k(\hat{\theta}) = z_k - N\big(\bar{U}_k - \bar{\phi}_k \hat{\theta}\big) \tag{8}$$

where

$$\bar{\phi}_k \triangleq \begin{bmatrix} \phi_{k-1} \\ \vdots \\ \phi_{k-l_f} \end{bmatrix} \in \mathbb{R}^{l_f l_u \times l_\theta}, \quad \bar{U}_k \triangleq \begin{bmatrix} u_{k-1} \\ \vdots \\ u_{k-l_f} \end{bmatrix} \in \mathbb{R}^{l_f l_u} \tag{9}$$

$$N \triangleq \begin{bmatrix} N_1 & \cdots & N_{l_f} \end{bmatrix} \in \mathbb{R}^{l_z \times l_f l_u}. \tag{10}$$

The choice of N includes all required modeling information. When the plant is SISO, that is, $l_z = l_u = 1$, this information consists of the sign of the leading numerator coefficient, the relative degree of the sampled-data system, and all nonminimum-phase (NMP) zeros [45], [46]. Since zeros are invariant under feedback, omission of an NMP zero from G_f may entail unstable pole-zero cancellation. Cancellation can be prevented, however, by using the control weighting R_u introduced next, as discussed in [45] and [49]. For SISO and multi-in multi-out (MIMO) systems, N can be constructed and updated online using data [46]. For simplicity in controlling the Rijke tube, which is an SISO system, we fix N and thus G_f prior to implementation.

Using (6), we define the cumulative cost function

$$J_k(\hat{\theta}) \triangleq \sum_{i=0}^{k} \Big[\hat{z}_i^{\mathsf{T}}(\hat{\theta})\hat{z}_i(\hat{\theta}) + \big(\phi_i \hat{\theta}\big)^{\mathsf{T}} R_u \phi_i \hat{\theta}\Big] + \big(\hat{\theta} - \theta_0\big)^{\mathsf{T}} P_0^{-1}\big(\hat{\theta} - \theta_0\big) \tag{11}$$

where $P_0 \in \mathbb{R}^{l_\theta \times l_\theta}$ is the positive definite and $R_u \in \mathbb{R}^{l_u \times l_u}$ is the positive semidefinite. As can be seen from (2), R_u serves as a control weighting, which prevents RCAC from canceling unmodeled NMP zeros, and the matrix P_0^{-1} defines the regularization term and initializes the recursion for P_k defined in the following.

The following result uses recursive least squares (RLS) [50], [51] to minimize (11), where, at each step k, the minimizer of (11) is the update θ_{k+1} of the controller coefficient vector.

Proposition 1: For all $k \geq 0$, the unique global minimizer θ_{k+1} of (11) is given by

$$P_{k+1} = P_k - P_k \begin{bmatrix} N\bar{\phi}_k \\ \phi_k \end{bmatrix}^{\mathsf{T}} \Gamma_k \begin{bmatrix} N\bar{\phi}_k \\ \phi_k \end{bmatrix} P_k \tag{12}$$

$$\theta_{k+1} = \theta_k - P_{k+1} \begin{bmatrix} N\bar{\phi}_k \\ \phi_k \end{bmatrix}^{\mathsf{T}} \bar{R} \begin{bmatrix} z_k - N\big(\bar{U}_k - \bar{\phi}_k \theta_k\big) \\ \phi_k \theta_k \end{bmatrix} \tag{13}$$

where

$$\Gamma_k \triangleq \bar{R} - \bar{R}\begin{bmatrix} N\bar{\phi}_k \\ \phi_k \end{bmatrix}\left(P_k^{-1} + \begin{bmatrix} N\bar{\phi}_k \\ \phi_k \end{bmatrix}^{\mathsf{T}} \bar{R} \begin{bmatrix} N\bar{\phi}_k \\ \phi_k \end{bmatrix}\right)^{-1} \begin{bmatrix} N\bar{\phi}_k \\ \phi_k \end{bmatrix}^{\mathsf{T}} \bar{R} \in \mathbb{R}^{(l_z+l_u)\times(l_z+l_u)} \tag{14}$$

$$\bar{R} \triangleq \operatorname{diag}\big(I_{l_z}, R_u\big) \in \mathbb{R}^{(l_z+l_u)\times(l_z+l_u)}. \tag{15}$$

For all of the numerical simulations and physical experiments in this article, θ_k is initialized as $\theta_0 = 0_{l_\theta \times 1}$ to reflect the absence of additional prior modeling information. Furthermore, except when specified otherwise, $G_f(\mathbf{q}) = -1/\mathbf{q}$, where the minus sign reflects sign information and the relative degree is set to 1. Aside from the selection of hyperparameters discussed next, no other modeling information is used by RCAC. For convenience, we set $P_0 = p_0 I_{l_\theta}$, where the scalar $p_0 > 0$ determines the initial rate of adaptation.

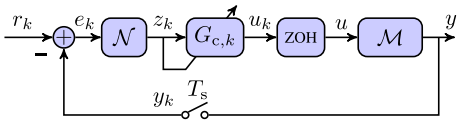

Fig. 2. Adaptive control of a continuous-time system $\mathcal{M}$. For this work, $r \equiv 0$ reflects the desire to suppress oscillations in the measured signal, $\mathcal{N}$ is the normalization function (16), and $\mathcal{M}$ represents the Rijke-tube model introduced in Section V for numerical simulations and the experimental Rijke-tube setup introduced in Section IV for physical experiments.

III. Sampled-Data Implementation of the Adaptive Control Law

For the experimental Rijke-tube setup, the adaptive controller is implemented as a sampled-data controller. Fig. 2 shows a block diagram of the sampled-data closed-loop system, where $y \in \mathbb{R}$ is the output of the continuous-time system $\mathcal{M}$, y_k is the sampled output, $r_k \in \mathbb{R}$ is the discrete-time command, $e_k \triangleq r_k - y_k$ is the command-following error, and $T_s > 0$ is the sampling period. For all adaptive controller experiments, $T_s = 0.001$ s/step. The digital-to-analog (D/A) and analog-to-digital (A/D) interfaces, which are synchronous, are zero-order hold (ZOH) and sampler, respectively. For this work, $r \equiv 0$ reflects the desire to suppress oscillations in the measured signal. Finally, $\mathcal{M}$ represents a Rijke-tube model introduced in Section V for numerical simulations and the experimental Rijke-tube setup introduced in Section IV for physical experiments.

The measured performance variable z_k, which is used for adaptation, is the normalized error

$$z_k \triangleq \mathcal{N}(e_k) \triangleq \frac{e_k}{1 + \nu|e_k|} \tag{16}$$

where $\nu \in [0, \infty)$. We fix $\nu = 0.2$ throughout this article. The adaptive controller $G_{c,k}$ operates on z_k to produce the discrete-time control $u_k \in \mathbb{R}$. Hence, $l_u = l_z = 1$. $G_{c,k}$ and u_k are updated at each sampling time $t_k \triangleq kT_s$.

In numerical simulations and physical experiments, the controller and adaptation are enabled and disabled in various ways. In particular, for the experimental scenarios, we consider the following modes of operation starting at step $k_0 \geq 0$.

1) *Mode 1:* The controller and adaptation are disabled. For all $k \geq k_0$, $u_k = 0$, $\theta_{k+1} = \theta_k$, and $P_{k+1} = P_k$.
2) *Mode 2:* The controller and adaptation are enabled. For all $k \geq k_0$, u_k, θ_{k+1}, and P_{k+1} are updated by (2), (12), and (13), respectively.
3) *Mode 3:* The controller is enabled, but adaptation is disabled, yielding a fixed-gain controller. For all $k \geq k_0$, u_k is updated by (2), $\theta_{k+1} = \theta_k$, and $P_{k+1} = P_k$.

Mode 1 is employed when the user requires that the open-loop system reach a desired behavior before control is applied, such as fully developed thermoacoustic oscillations. Mode 2 corresponds to the normal operation of the adaptive controller. Mode 3 is useful for probing the properties of the controller at a given time step; in effect, at step k, the gains of $G_{c,k}$ are frozen, and the controller operates as a fixed-gain controller, called the frozen-gain adaptive controller.

Implementation of the adaptive controller requires selection of the closed-loop target model G_f, which captures the properties mentioned in Section II [45]. In addition, the hyperparameters l_c, p_0, and R_u must be selected depending on the system and performance requirements. Note that R_u is scalar since $l_u = 1$. As mentioned in Section I, all of these quantities are selected for the experimental Rijke-tube setup after performing closed-loop numerical simulations with an emulation model.

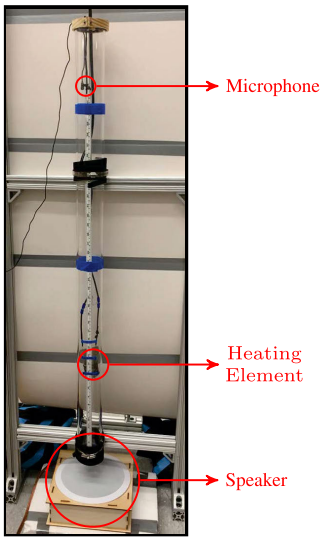

Fig. 3. Experimental Rijke-tube setup. The heating element can be raised or lowered by a dc motor (not shown) to vary the dynamics of the system.

IV. Description of the Experimental Rijke-Tube Setup

The experimental Rijke-tube setup built is shown in Fig. 3, where a heating element is placed inside a vertical Pyrex tube whose length is 1.2 m and inner cross-sectional area is 4.6×10^{-3} m^2, similar to the setup in [1]. The heating element is a coil made from 22-gauge Kanthal wire with a resistance of 22 Ω. The coil is attached by a Kevlar rope to a dc motor, which is used to reposition the coil. A Variac is used as a power supply to control the voltage supplied to the coil. To measure pressure oscillations, a microphone is placed at the top of the tube and connected to a preamplifier. The microphone was calibrated using a sound pressure level meter to convert voltage measurements to pascals (Pa). To provide the control input, a speaker is placed at the bottom of the tube and connected to an amplifier. Note that, since the speaker and microphone are not colocated, the linearized plant dynamics have NMP zeros, as shown in [1]. Consequently, passivity arguments cannot be used to guarantee closed-loop stability.

Pressure oscillations are created within the experimental Rijke-tube setup by supplying voltage to the heating element, as noted by Rijke [19] and subsequently elucidated by Rayleigh [20] and Sarpotdar [52]. As explained in [52], [53], [54], and [55, pp. 232–234], pressure oscillations are created and become self-excited if and only if the heating element is placed in the lower half of the tube and sufficient power is provided to the heating element to overcome the acoustic damping. Furthermore, pressure oscillations are more easily created when the heat source is placed at one quarter of the

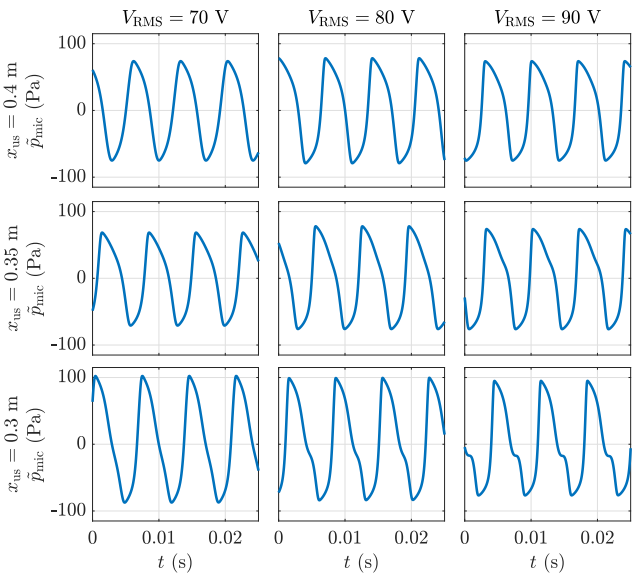

Fig. 4. Pressure measurements from the open-loop experimental Rijke-tube setup obtained at the coil positions $x_{\text{us}} \in \{0.3, 0.35, 0.4\}$ m and the ac voltage levels $V_{\text{rms}} \in \{70, 80, 90\}$ V, where x_{us} is the distance of the coil from the bottom of the tube and V_{rms} is the root-mean-square (rms) voltage provided by the Variac.

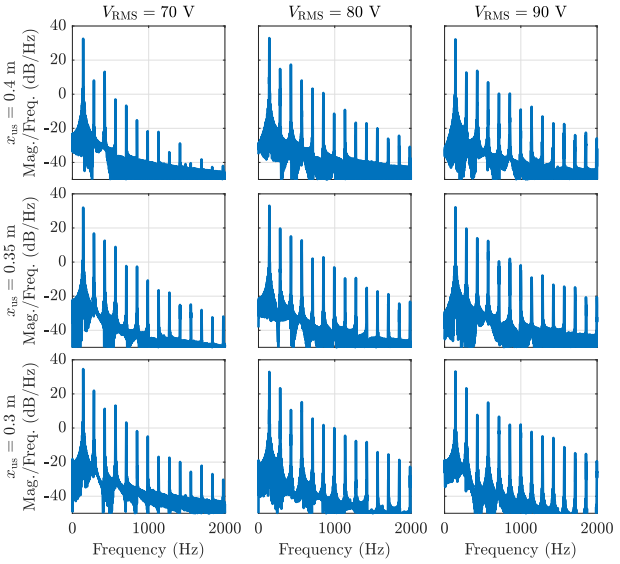

Fig. 5. Amplitude spectra of the pressure measurements from the open-loop experiment at each setting considered in Fig. 4.

length of the tube from its bottom and become harder to create as the heat source is moved from this position [52]. The chosen experimental Rijke-tube setup exhibits thermoacoustic oscillations, whose characteristics depend on the vertical position of the heating element and the voltage provided to the heating element, as shown in Figs. 4 and 5.

V. Physics-Based Model of the Rijke Tube

A schematic of the experimental Rijke-tube setup is shown in Fig. 6. The tube has length L and cross-sectional area A. The heating element is positioned x_{ds} m below the top of the tube and x_{us} m above the bottom of the tube; note that $L = x_{\text{ds}} + x_{\text{us}}$. The microphone is positioned x_{mic} m

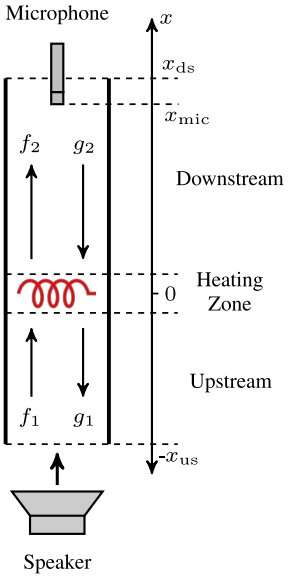

Fig. 6. Schematic of the Rijke-tube model.

above the heating element, and the speaker is placed below the tube. In Fig. 6, f_1 and g_1 represent the bidirectional acoustic pressure propagation in the upstream portion of the tube, and f_2 and g_2 represent the bidirectional acoustic pressure propagation in the downstream portion of the tube.

The Rijke-tube model (28)–(31) is based on the ducted-flame model given in [56] and further developed in [29] and [35]. A key difference between the models developed in [56] and the models developed in [29] and [35] is that, in [56], a nonlinearity is added before the linear flame dynamics. This feature is included in (28)–(31), where the saturation function used in [56] is replaced by a hyperbolic tangent to improve numerical stability. Note that these nonlinearities are distinct from the square-root function used in [1] within the context of a different model. Let $x \in [-x_{\text{us}}, x_{\text{ds}}]$ denote a position within the tube in m, where $x = 0$ m is the position of the heating element in the tube. Let p and v be the airflow pressure and velocity, respectively, such that

$$p(t,x) \triangleq \begin{cases} \bar{p}_1 + \tilde{p}_1(t,x), & x \in [-x_{\text{us}}, 0] \\ \bar{p}_2 + \tilde{p}_2(t,x), & x \in (0, x_{\text{ds}}] \end{cases} \tag{17}$$

$$v(t,x) \triangleq \begin{cases} \bar{v}_1 + \tilde{v}_1(t,x), & x \in [-x_{\text{us}}, 0] \\ \bar{v}_2 + \tilde{v}_2(t,x), & x \in (0, x_{\text{ds}}] \end{cases} \tag{18}$$

where $\bar{p}_1, \bar{p}_2 > 0$ are the mean airflow pressure in the upstream and downstream portions, respectively, $\bar{v}_1, \bar{v}_2 > 0$ are the mean airflow velocities in the upstream and downstream portions, respectively, and, for all $i \in \{1, 2\}$

$$\tilde{p}_i(t,x) \triangleq f_i\left(t - \tfrac{x}{\bar{c}_i}\right) + g_i\left(t + \tfrac{x}{\bar{c}_i}\right) \tag{19}$$

$$\tilde{v}_i(t,x) \triangleq \tfrac{1}{\bar{\rho}_i \bar{c}_i}\left[f_i\left(t - \tfrac{x}{\bar{c}_i}\right) - g_i\left(t + \tfrac{x}{\bar{c}_i}\right)\right] \tag{20}$$

where $\bar{c}_1, \bar{c}_2 > 0$ are the mean wave speeds in the upstream and downstream portions, respectively, and $\bar{\rho}_1, \bar{\rho}_2 > 0$ are the mean air densities in the upstream and downstream portions,

respectively. Furthermore, f_1 and g_2 are given by

$$f_1(t) = R_{\rm us} g_1(t - \tau_{\rm us}) + \tilde{p}_{\rm spk}\left(t - \tfrac{\tau_{\rm us}}{2}\right) \tag{21}$$

$$g_2(t) = R_{\rm ds} f_2(t - \tau_{\rm ds}) \tag{22}$$

where $R_{\rm us}, R_{\rm ds} \in \mathbb{R}$ are reflection coefficients, $\tau_{\rm us} \triangleq (2x_{\rm us}/\bar{c}_1)$ and $\tau_{\rm ds} \triangleq (2x_{\rm ds}/\bar{c}_2)$, and $\tilde{p}_{\rm spk} \in \mathbb{R}$ is the speaker pressure.

Next, the dynamics of the heat release rate perturbations of the coil $\tilde{Q}$ are modeled by

$$b\dot{\tilde{Q}}(t) + \tilde{Q}(t) = a\psi\big(\tilde{v}_1(t,0)\big) \tag{23}$$

where $a, b \in (0, \infty)$ and $\psi : \mathbb{R} \to \mathbb{R}$ is given by

$$\psi\big(\tilde{v}_1(t,0)\big) \triangleq \delta \tanh\big(\eta \tilde{v}_1(t,0)\big) \tag{24}$$

where $\delta, \eta \in (0, \infty)$. Then, define

$$F \triangleq X^{-1}\begin{bmatrix} Y & 0 \\ & \frac{1}{A\bar{c}_1} \end{bmatrix} \in \mathbb{R}^{2\times 3}$$

where $X, Y \in \mathbb{R}^{2\times 2}$, and let g_1 and f_2 be given by

$$\begin{bmatrix} g_1(t) \\ f_2(t) \end{bmatrix} = F \begin{bmatrix} f_1(t) \\ g_2(t) \\ \tilde{Q}(t) \end{bmatrix}. \tag{25}$$

Since the Mach numbers are assumed to be low [29], [35], it follows from the expressions for X and Y given in [56, Appendix] that

$$X \triangleq \begin{bmatrix} -1 & 1 \\ \frac{1}{\bar{\gamma}-1} & \frac{\bar{c}_2}{\bar{c}_1}\frac{1}{\bar{\gamma}-1} \end{bmatrix}, \qquad Y \triangleq \begin{bmatrix} 1 & -1 \\ \frac{1}{\bar{\gamma}-1} & \frac{\bar{c}_2}{\bar{c}_1}\frac{1}{\bar{\gamma}-1} \end{bmatrix} \tag{26}$$

where $\bar{\gamma}$ is the adiabatic ratio of dry air at room temperature. Finally, the acoustic pressure $\tilde{p}_{\rm mic}$ measured by the microphone is given by

$$\begin{aligned} \tilde{p}_{\rm mic}(t) \triangleq \tilde{p}_2(t, x_{\rm mic}) &= f_2\left(t - \tfrac{x_{\rm mic}}{\bar{c}_2}\right) + g_2\left(t + \tfrac{x_{\rm mic}}{\bar{c}_2}\right) \\ &= f_2(t - \tau_{\rm mic}) + R_{\rm ds} f_2(t - (\tau_{\rm ds} - \tau_{\rm mic})) \end{aligned} \tag{27}$$

where $\tau_{\rm mic} \triangleq (x_{\rm mic}/\bar{c}_2)$.

The block diagram in Fig. 7 summarizes the dynamics of the Rijke-tube model, where the control input $u = \tilde{p}_{\rm spk}$ is the speaker pressure, and the measurement $y = \tilde{p}_{\rm mic}$ is the microphone signal. These dynamics can be written as

$$\dot{\tilde{Q}}(t) = -\frac{1}{b}\tilde{Q}(t) + \frac{a}{b}\psi\big(\tilde{v}_1(t,0)\big) \tag{28}$$

$$\tilde{v}_1(t,0) = \frac{1}{\bar{\rho}_1\bar{c}_1}\begin{bmatrix} 1 & -1 & R_{\rm us} \end{bmatrix}\begin{bmatrix} \tilde{p}_{\rm spk}(t - \tau_{\rm us}/2) \\ g_1(t) \\ g_1(t - \tau_{\rm us}) \end{bmatrix} \tag{29}$$

$$\begin{bmatrix} g_1(t) \\ f_2(t) \end{bmatrix} = F \begin{bmatrix} 1 & 0 & 0 & 0 \\ 0 & 1 & R_{\rm us} & 0 \\ 0 & 0 & 0 & R_{\rm ds} \end{bmatrix}\begin{bmatrix} \tilde{Q}(t) \\ \tilde{p}_{\rm spk}(t - \tau_{\rm us}/2) \\ g_1(t - \tau_{\rm us}) \\ f_2(t - \tau_{\rm ds}) \end{bmatrix} \tag{30}$$

$$\tilde{p}_{\rm mic}(t) = \begin{bmatrix} 1 & R_{\rm ds} \end{bmatrix}\begin{bmatrix} f_2(t - \tau_{\rm mic}) \\ f_2(t - (\tau_{\rm ds} - \tau_{\rm mic})) \end{bmatrix}. \tag{31}$$

Note that (28)–(31) are delay differential equations (DDEs) with state $\tilde{Q}$, input $\tilde{p}_{\rm spk}$, output $\tilde{p}_{\rm mic}$, and time-varying parameters g_1 and f_2. Furthermore, the placement of the speaker and the microphone relative to the coil results in input and output time delays, as shown in (30) and (31) and Fig. 7.

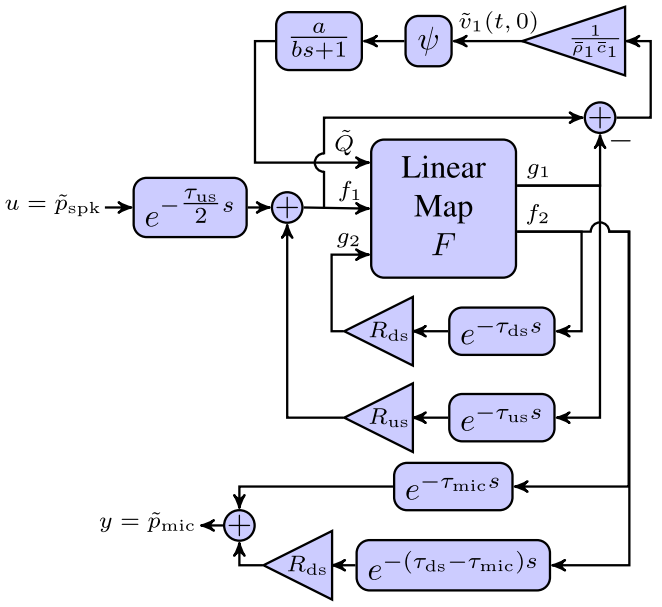

Fig. 7. Block diagram of the Rijke-tube model. The control input $u = \tilde{p}_{\rm spk}$ is the speaker pressure, and the microphone signal $y = \tilde{p}_{\rm mic}$ is the measurement. This block diagram is executed in Simulink.

VI. Rijke-Tube Model Parameter Fit

The parameters for the Rijke-tube model introduced in Section V and shown in Fig. 7 are chosen to emulate the characteristics of the experimental Rijke-tube setup. In particular, with the coil placed 0.4 m above the bottom of the tube and the root-mean-square (rms) Variac voltage set to $V_{\rm rms} = 70$ V, the emulation model captures the amplitude and frequency of the highest magnitude of the spectrum of the pressure measurements obtained from open-loop experiments. The constants $\bar{\rho}_1$ and $\bar{\gamma}$ denote the density and adiabatic ratio of dry air at room temperature, respectively, $\bar{c}_1$ and $\bar{c}_2$ are chosen as in [35], and $x_{\rm us}, x_{\rm ds}$, and $x_{\rm mic}$ are based on the configuration used in open-loop experiments. Hence, $L = 1.2$ m, $x_{\rm us} = 0.4$ m, and $x_{\rm ds} = 1.2$ m $- 0.4$ m $= 0.8$ m. Since the microphone is placed approximately 0.1 m below the top of the tube, $x_{\rm mic} = x_{\rm ds} - 0.1$ m $= 0.7$ m. $R_{\rm us}$ and $R_{\rm ds}$ are fixed to values that induce a self-excited response in the model output more easily. Then, a b, δ, and η are manually adjusted to match the pressure measurements obtained from the open-loop experiments. The chosen parameters for the Rijke-tube emulation model are shown in Table I.

Numerical simulations of the emulation model are performed in Simulink using fixed-step integration with a step size 10^{-4} s/step, that is, $T_{\rm s}/10$. Linear interpolation is used to calculate the delayed values of $\tilde{p}_{\rm spk}$, g_1, and f_2. For all $t \le 0$, $\tilde{p}_{\rm spk}(t) = g_1(t) = f_2(t) = 0$. The value of $\tilde{Q}(0)$ is randomly selected and provides the initial disturbance to generate the oscillations.

The open-loop ($u \equiv 0$) response of the emulation model and the experimental data is shown in Fig. 8. The highest magnitude peaks of the amplitude spectra of the open-loop experiment and the emulation model match at 140 Hz, as shown in Fig. 8. As can be seen, the magnitude peaks of the amplitude spectrum of the emulation model match

TABLE I
PARAMETERS OF THE RIJKE-TUBE EMULATION MODEL

Parameter	Value	Units	Comment
$\bar{\rho}_1$	1.225	kg/m^3	Based on the experimental Rijke-tube setup
$\bar{\gamma}$	1.4	–	
$\bar{c}_1$	340	m/s	
$\bar{c}_2$	360	m/s	
A	$4.6 \cdot 10^{-3}$	m^2	
L	1.2	m	
x_{us}	0.4	m	
x_{ds}	$L - x_{\text{us}}$	m	
x_{mic}	$x_{\text{ds}} - 0.1$	m	
R_{us}	-0.99	–	Based on open-loop pressure measurements
R_{ds}	-0.99	–	
a	375	–	
b	$2 \cdot 10^{-3}$	–	
δ	0.1128	m/s	
η	3.21	–	

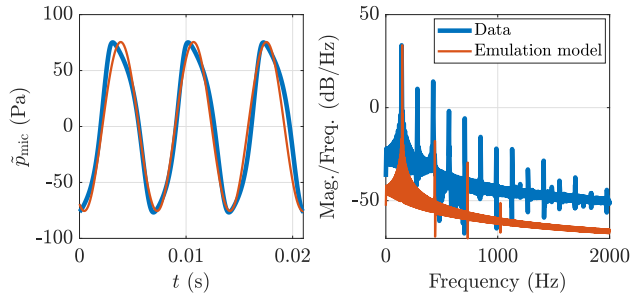

Fig. 8. Comparison of the time responses and amplitude spectra of the open-loop experiment and the emulation model. Note that the amplitude spectra of the data and emulation model match only at the first peak. The parameters used for the emulation model are given in Table I.

only the peaks corresponding to the odd harmonics of the amplitude spectrum of the open-loop experiment. Although this mismatch is inconsistent with the reflection coefficients R_{us} and R_{ds}, which model open–open boundary conditions, the predictions of a linear acoustic model are not valid for the emulation model, which is nonlinear. While the emulation model output only roughly matches the data, Section VIII-A shows that this emulation model is sufficient for hyperparameter tuning.

VII. NUMERICAL SIMULATION OF THE RIJKE-TUBE MODEL FOR HYPERPARAMETER SELECTION

In this section, the emulation model is used to select hyperparameters such that the adaptive controller suppresses the self-excited response of the Rijke-tube emulation model in three cases, where the heating element is placed at three different positions along the tube by changing the positive values of x_{ds} and x_{us}, such that $x_{\text{us}} \in \{0.3, 0.35, 0.4\}$ m and $x_{\text{ds}} = L - x_{\text{us}}$. Hence, the parameters used for the emulation model are given in Table I, except for x_{us}, for which three different values are considered. As mentioned in Section II, $G_{\text{f}}(\mathbf{q}) = -1/\mathbf{q}$, and thus, $l_{\text{f}} = 1$ and $N = N_1 = -1$. Hence, only l_{c}, p_0, and R_u need to be selected. As mentioned in Section I, the level of suppression of the thermoacoustic oscillations, referred to as oscillation suppression,

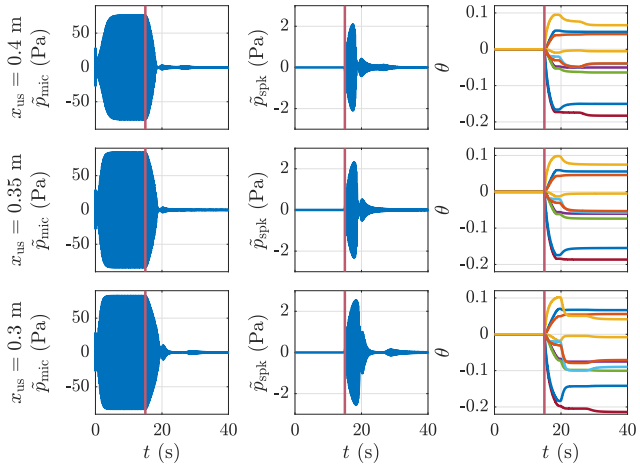

Fig. 9. Adaptive control of the simulated Rijke-tube model. The experiment transitions from Mode 1 to Mode 2 at $t = 15$ s, as indicated by the red vertical lines. Each row shows the responses for $x_{\text{us}} \in \{0.3, 0.35, 0.4\}$ m, for $t \in [0, 40]$ s. The first, second, and third columns show the pressure measurements $\tilde{p}_{\text{mic}}$, the requested speaker pressure $\tilde{p}_{\text{spk}}$, and the adaptive controller coefficients θ, respectively.

is used to evaluate the performance of the controller, which is defined to be the ratio of the steady-state open-loop maximum time-domain pressure amplitude to the steady-state closed-loop maximum time-domain pressure amplitude in dB.

The controller initially operates in Mode 1, and the experiment transitions to Mode 2 at $t = 15$ s, which is sufficient time for the oscillatory response of the open-loop models to fully develop. Several simulations are performed, in which the hyperparameters l_{c}, p_0, and R_u are manually adjusted until at least 40 dB of oscillation suppression is obtained across all scenarios ($x_{\text{us}} \in \{0.3, 0.35, 0.4\}$ m). The selected hyperparameters are given by $l_{\text{c}} = 5$, $p_0 = 10^{-5}$, and $R_u = 1$.

The results of the numerical simulations using the selected hyperparameters are shown in Figs. 9–12. Fig. 9 shows that, in all cases, the adaptive controller suppresses the oscillations; in particular, for $x_{\text{us}} \in \{0.4, 0.35, 0.3\}$ m, the adaptive controller suppresses the oscillations by 72.74, 59.63, and 54.70 dB, respectively. Fig. 10 shows that, in all cases, the adaptive controller suppresses the highest magnitude peak of the amplitude spectra corresponding to the open-loop response of the emulation model. Fig. 11 shows that the poles of the adaptive controller evolve in a similar manner in all cases. In contrast, the zeros evolve differently in different cases, which shows that the response of the adaptive controller depends on the operating conditions. Note that none of the poles lie close to the unit circle, which shows that, in contrast to the standard approach for harmonic disturbance rejection in linear systems, the adaptive controller does not exploit an internal-model strategy for oscillation suppression [57]. Furthermore, Fig. 12 shows that the magnitude of the adaptive controller indicates high gain near $\pi/4$ rad/sample, which is equivalent to 125 Hz given T_{s}. The high-gain response of the adaptive controller thus corresponds to the first harmonic of the open-loop amplitude spectra, which occurs near 140 Hz, as shown in Fig. 10. The hyperparameters used in these examples are initially used in the physical experiments.

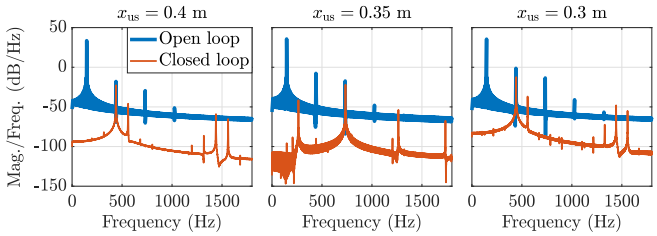

Fig. 10. Amplitude spectra of the simulated Rijke-tube model. The amplitude spectra of the pressure measurements obtained from the open-loop simulations and the closed-loop simulations using the adaptive controller are shown for $x_{us} \in \{0.3, 0.35, 0.4\}$ m.

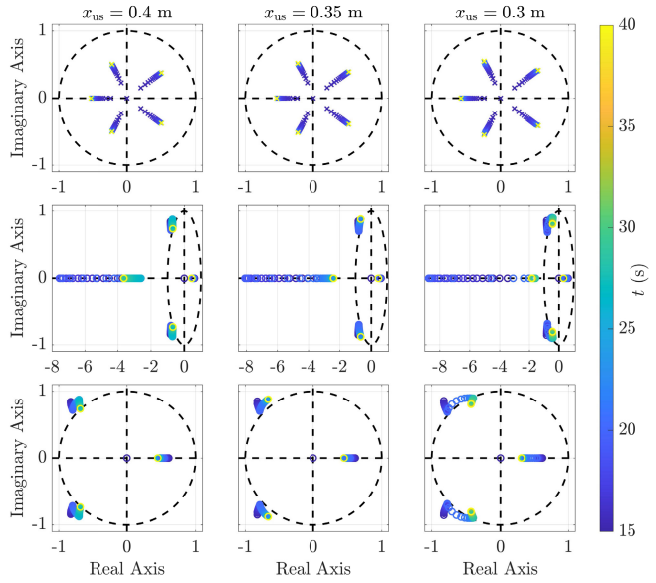

Fig. 11. Evolution of the poles and zeros of the adaptive controller during the simulation of the closed-loop system with the Rijke-tube model. Each column shows the poles and zeros for $x_{us} \in \{0.3, 0.35, 0.4\}$ m and $t \in [15, 40]$ s. The top row displays the poles as crosses, the middle row displays the zeros as circles, and the bottom row shows zoomed-in versions of the plots in the middle row.

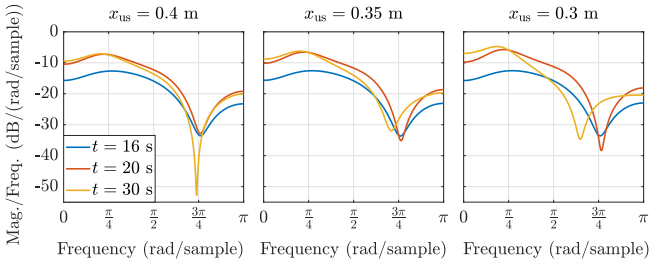

Fig. 12. Evolution of the frequency response of the adaptive controller during the simulation of the closed-loop system with the Rijke-tube model. The magnitude responses of the adaptive controller are shown for $x_{us} \in \{0.3, 0.35, 0.4\}$ m and $t \in \{16, 20, 30\}$ s.

VIII. Physical Adaptive Control Experiments

The closed-loop experimental Rijke-tube setup shown in Fig. 13 is used in the following to perform physical adaptive control experiments. The hyperparameters determined in Section VII are initially used for the adaptive controller. In particular, Section VIII-A shows experiments in which the Rijke-tube setup parameters are kept constant,

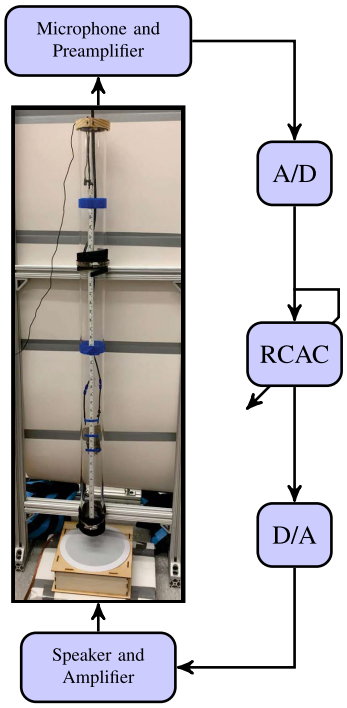

Fig. 13. Experimental closed-loop Rijke-tube setup.

Section VIII-B shows the effects of hyperparameter perturbation on the RCAC rate of adaptation and suppression performance, Section VIII-C evaluates the suppression performance of the frozen-gain adaptive controller resulting from an initial implementation of RCAC, Section VIII-D shows experiments in which the parameters of the Rijke-tube setup are modified during closed-loop operation, and Sections VIII-E and VIII-F provide experiment-based stability analyses of RCAC.

A. Rijke-Tube Fixed-Parameter Experiments

We now consider experimental scenarios where the coil position and supplied voltage are kept constant. In total, nine combinations are considered such that $x_{us} \in \{0.3, 0.35, 0.4\}$ m and $V_{RMS} \in \{70, 80, 90\}$ V, which are the cases shown in Figs. 4 and 5. Through testing, it is determined that the oscillations are more difficult to suppress as x_{us} moves closer to 0.3 m (a quarter of the tube length from its bottom, as mentioned in Section IV) and V_{RMS} increases. The experiment begins in Mode 1 and transitions to Mode 2 after the oscillations are formed.

Since it is mentioned in [1] and [35] that a constant-gain proportional controller can be used to suppress the oscillations, the constant-gain proportional controller in Fig. 14 is also implemented for comparison, where K is the constant proportional gain and the sampling rate is $T_s/20$ s/step. A small sampling rate is chosen to allow the digital computer to better approximate the continuous-time implementations considered in [1] and [35]. For all $k \geq 0$, $u_k = 0$ in the case where the constant-gain proportional controller is disabled and $u_k = Ke_k$ in the case where the constant-gain proportional controller is enabled. The constant-gain proportional controller is used in the four corner cases of the nine cases considered, using

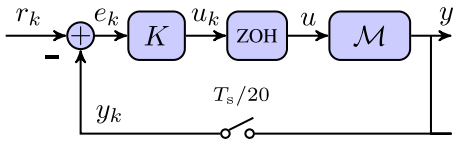

Fig. 14. Constant-gain proportional control of the continuous-time system $\mathcal{M}$. For this work, $r \equiv 0$ reflects the desire to suppress oscillations in the measured signal. $\mathcal{M}$ represents the experimental Rijke-tube setup.

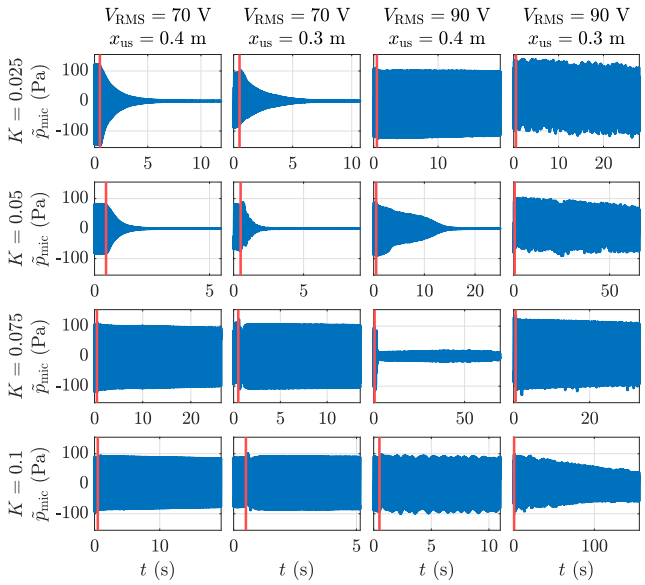

Fig. 15. Rijke-tube fixed-parameter experiments. Pressure measurements $\tilde{p}_{\text{mic}}$ from the closed-loop experiments using the constant-gain proportional controller in Fig. 14 are shown for $x_{\text{us}} \in \{0.3, 0.4\}$ m, $V_{\text{rms}} \in \{70, 90\}$ V, and $K \in \{0.025, 0.05, 0.075, 0.01\}$. The constant-gain proportional controller is initially disabled and is enabled at the time indicated by the red vertical lines. In order to render the details discernible, different time windows are used in each plot.

four different values of K. The results of the suppression experiments with the constant-gain proportional controller in Fig. 14 for $x_{\text{us}} \in \{0.3, 0.4\}$ m, $V_{\text{rms}} \in \{70, 90\}$ V, and $K \in \{0.025, 0.05, 0.075, 0.01\}$ are shown in Fig. 15. In all of these experiments, the oscillation suppression is at most 45.73 dB, and no suppression is achieved in nine cases.

For the adaptive controller implementation, the hyperparameters are the same as the ones determined from the numerical simulations using the emulation model, that is, $l_c = 5$, $p_0 = 10^{-5}$, $R_u = 1$, and $G_f(\mathbf{q}) = -1/\mathbf{q}$. The results of the adaptive suppression experiments for $x_{\text{us}} \in \{0.3, 0.35, 0.4\}$ m and $V_{\text{rms}} \in \{70, 80, 90\}$ V are shown in Figs. 16–20. In all of these experiments, the oscillation suppression is at least 45.85 dB. Hence, as in Section VII, oscillation suppression greater than 45 dB is achieved using the same hyperparameters in all tests. Furthermore, Fig. 20 shows that the magnitude of the adaptive controller indicates high gain near $\pi/4$ rad/sample, which is equivalent to 125 Hz given T_s. The high-gain response of the adaptive controller thus corresponds to the first harmonic of the open-loop amplitude spectra, which occurs near 140 Hz, as shown in Fig. 17 and similar to Section VII.

B. Hyperparameter Perturbation Experiments

We now consider experimental scenarios where the hyperparameters p_0 and R_u are modified, starting from the values

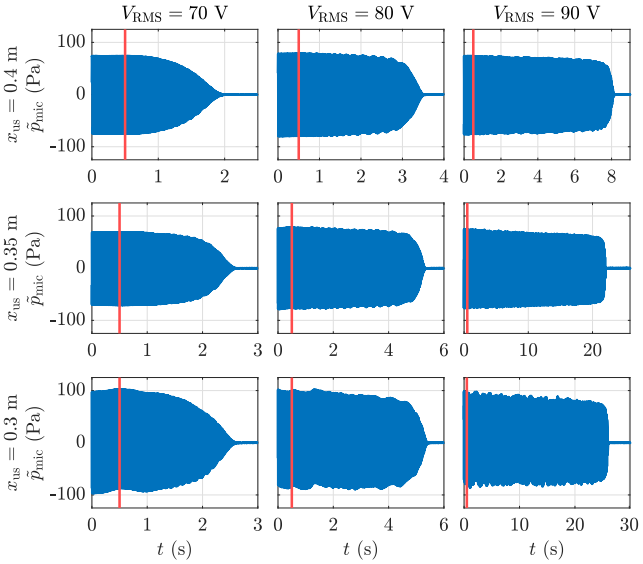

Fig. 16. Rijke-tube fixed-parameter experiments. Pressure measurements $\tilde{p}_{\text{mic}}$ from the closed-loop experiments using the adaptive controller are shown for $x_{\text{us}} \in \{0.3, 0.35, 0.4\}$ m and $V_{\text{rms}} \in \{70, 80, 90\}$ V. Each experiment transitions from Mode 1 to Mode 2 at the time indicated by the red vertical line. The same hyperparameters are used in all tests.

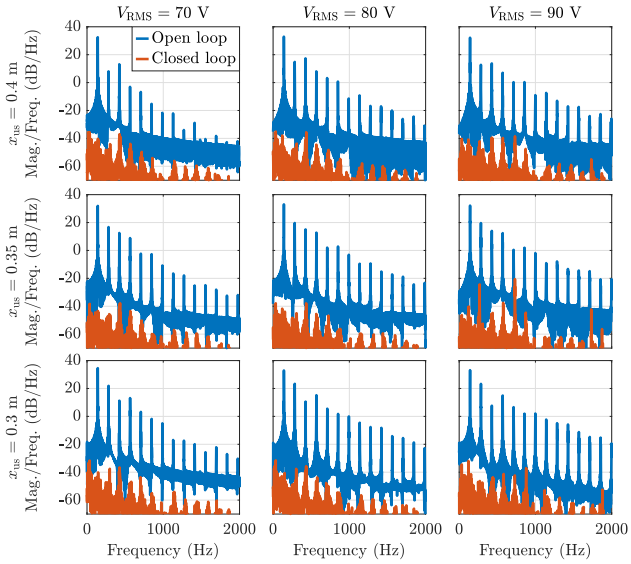

Fig. 17. Rijke-tube fixed-parameter experiments. Amplitude spectra of the experimental Rijke-tube setup. The amplitude spectra of the pressure measurements obtained from the open-loop experiments and the closed-loop experiments using the adaptive controller are shown for $x_{\text{us}} \in \{0.3, 0.35, 0.4\}$ m and $V_{\text{rms}} \in \{70, 80, 90\}$ V. The same hyperparameters are used in all closed-loop tests.

determined in Section VII. In particular, the adaptive controller is implemented in the case where $x_{\text{us}} = 0.3$ m and $V_{\text{rms}} = 90$ V for $p_0 \in \{10^{-5}, 10^{-4}, 10^{-3}\}$ and $R_u \in \{0.5, 0.75, 1\}$. As in Section VIII-A, $l_c = 5$ and $G_f(\mathbf{q}) = -1/\mathbf{q}$. The experiment begins in Mode 1 and transitions to Mode 2 after the oscillations are established.

The results for all hyperparameter combinations are shown in Figs. 21–24. In all of these experiments, the oscillation suppression is at least 31.13 dB. Furthermore, Fig. 24 shows that, for all hyperparameter combinations, the magnitude of

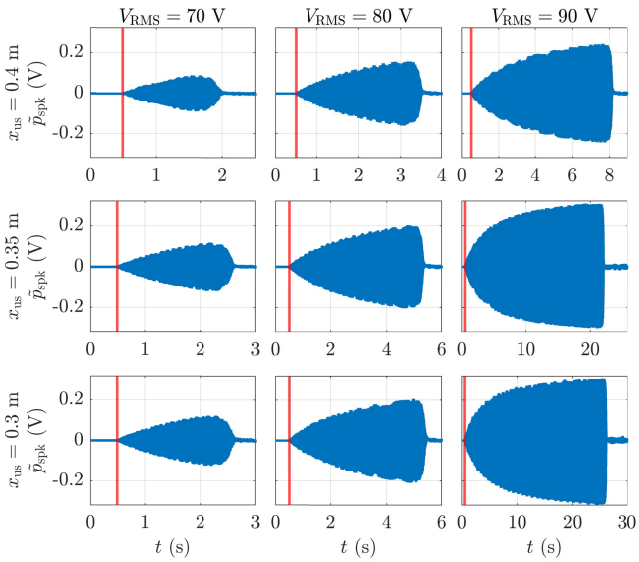

Fig. 18. Rijke-tube fixed-parameter experiments. The requested speaker voltage $\tilde{p}_{\mathrm{spk}}$ from the closed-loop experiments using the adaptive controller is shown for $x_{\mathrm{us}} \in \{0.3, 0.35, 0.4\}$ m and $V_{\mathrm{rms}} \in \{70, 80, 90\}$ V. Each experiment transitions from Mode 1 to Mode 2 at the time indicated by the red vertical line. The same hyperparameters are used in all tests.

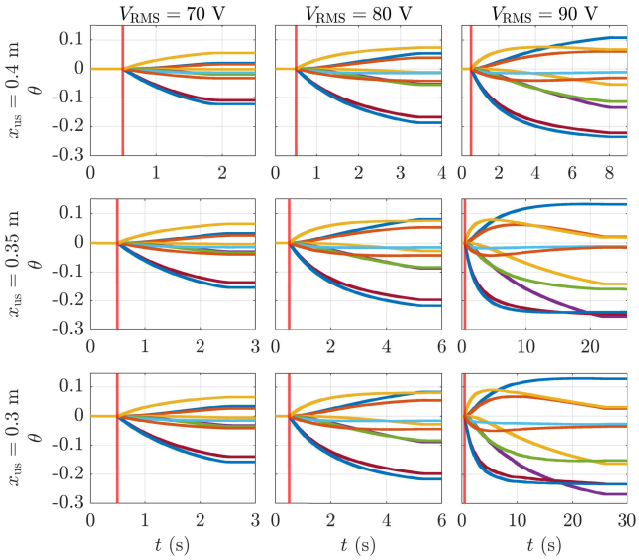

Fig. 19. Rijke-tube fixed-parameter experiments. The controller coefficients θ from the closed-loop experiments using the adaptive controller are shown for $x_{\mathrm{us}} \in \{0.3, 0.35, 0.4\}$ m and $V_{\mathrm{rms}} \in \{70, 80, 90\}$ V. Each experiment transitions from Mode 1 to Mode 2 at the time indicated by the red vertical line. The same hyperparameters are used in all tests.

the adaptive controller indicates a gain higher than 0 dB near $\pi/4$ rad/sample. Note that increasing p_0 and decreasing R_u results in faster suppression, as shown in Fig. 21, which requires larger speaker signal amplitudes, as shown in Fig. 22.

C. Performance Evaluation of the Frozen-Gain Adaptive Controller

We now consider experimental scenarios where the adaptive controller coefficients are saved and used to implement a frozen-gain adaptive controller in subsequent experiments. This experiment is conducted for $x_{\mathrm{us}} = 0.3$ m and $V_{\mathrm{rms}} = 90$ V.

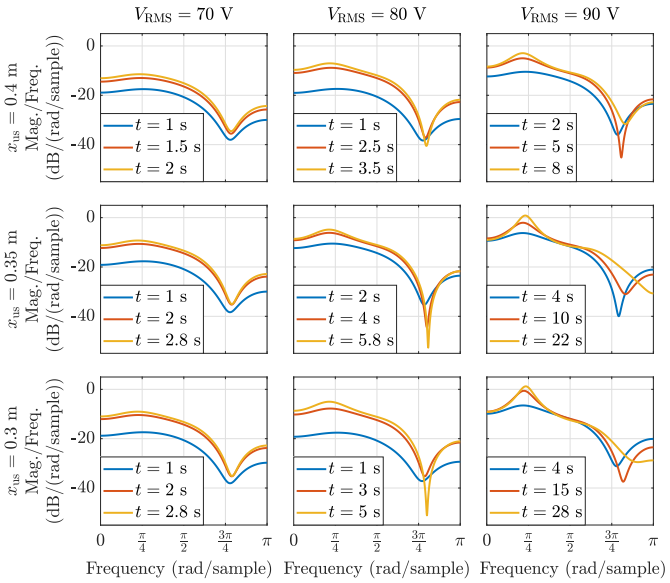

Fig. 20. Rijke-tube fixed-parameter experiments. The magnitude responses of the adaptive controller from the closed-loop experiments are shown for $x_{\mathrm{us}} \in \{0.3, 0.35, 0.4\}$ m, $V_{\mathrm{rms}} \in \{70, 80, 90\}$ V, and the times indicated in each legend. The same hyperparameters are used in all tests.

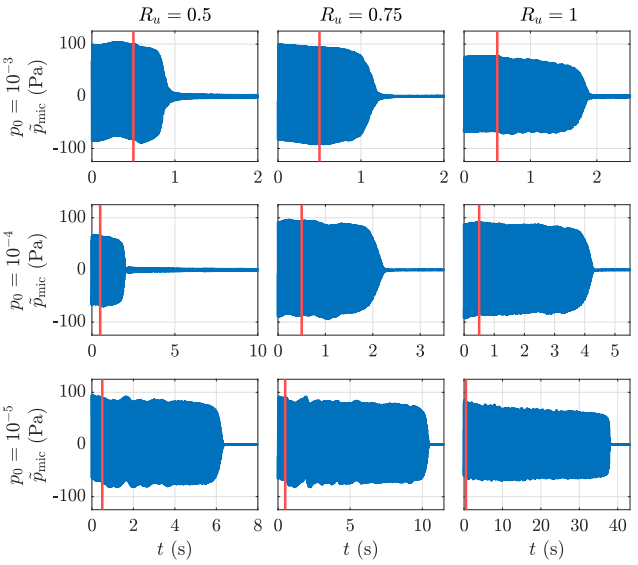

Fig. 21. Hyperparameter perturbation experiments. Pressure measurements $\tilde{p}_{\mathrm{mic}}$ from the closed-loop experiments using the adaptive controller are shown for $x_{\mathrm{us}} = 0.3$ m, $V_{\mathrm{rms}} = 90$ V, $p_0 \in \{10^{-5}, 10^{-4}, 10^{-3}\}$, and $R_u \in \{0.5, 0.75, 1\}$. Each experiment transitions from Mode 1 to Mode 2 at the time indicated by the red vertical line.

The following procedure consisting of five phases is given as follows.

1) *Phase 1:* The experiment begins in Mode 1.
2) *Phase 2:* The experiment transitions to Mode 2 after the oscillations are formed.
3) *Phase 3:* After no further oscillation suppression is achieved, the experiment transitions to Mode 3.
4) *Phase 4:* After some time, the experiment transitions to Mode 1, which allows the oscillations to recover their open-loop amplitude.

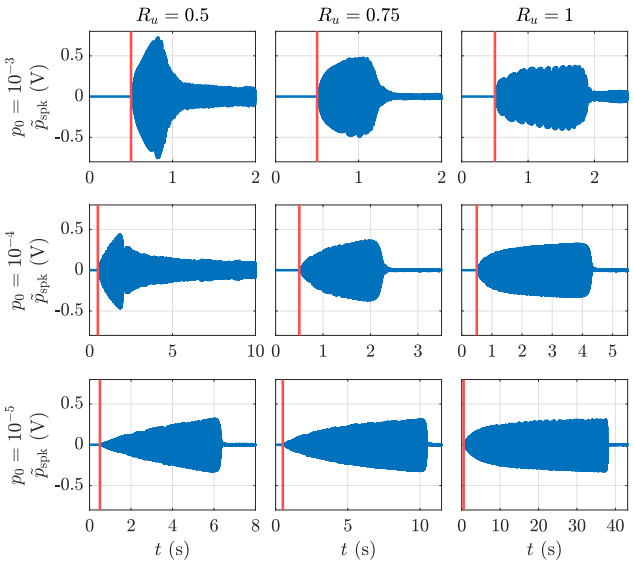

Fig. 22. Hyperparameter perturbation experiments. Requested speaker voltage $\tilde{p}_{\text{spk}}$ from the closed-loop experiments using the adaptive controller is shown for $x_{\text{us}} = 0.3$ m, $V_{\text{rms}} = 90$ V, $p_0 \in \{10^{-5}, 10^{-4}, 10^{-3}\}$, and $R_u \in \{0.5, 0.75, 1\}$. Each experiment transitions from Mode 1 to Mode 2 at the time indicated by the red vertical line.

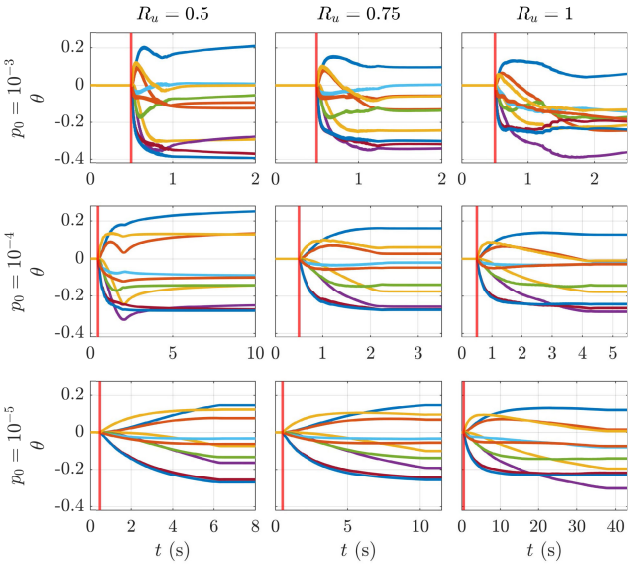

Fig. 23. Hyperparameter perturbation experiments. The controller coefficients θ from the closed-loop experiments using the adaptive controller are shown for $x_{\text{us}} = 0.3$ m, $V_{\text{rms}} = 90$ V, $p_0 \in \{10^{-5}, 10^{-4}, 10^{-3}\}$, and $R_u \in \{0.5, 0.75, 1\}$. Each experiment transitions from Mode 1 to Mode 2 at the time indicated by the red vertical line.

5) *Phase 5:* After the oscillations recover their open-loop amplitude, the experiment transitions to Mode 3.

For this test, $l_{\text{c}} = 5$, $p_0 = 10^{-4}$, $R_u = 0.75$, and $G_{\text{f}}(\mathbf{q}) = -1/\mathbf{q}$ are used. Note that the values of p_0 and R_u are changed from those determined in Section VII since the results of Section VIII-B showed that these hyperparameters yield faster suppression.

The experimental results are shown in Fig. 25. At the end of Phase 2, the adaptive controller suppresses oscillations by 43.75 dB. At the end of Phase 5, the frozen-gain adaptive controller suppresses the oscillations by 45.31 dB.

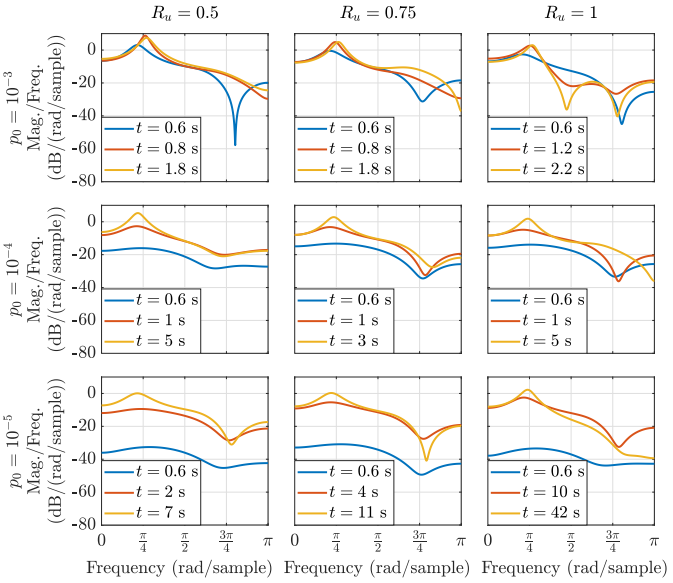

Fig. 24. Hyperparameter perturbation experiments. The magnitude responses of the adaptive controller from the closed-loop experiments are shown for $x_{\text{us}} = 0.3$ m, $V_{\text{rms}} = 90$ V, $p_0 \in \{10^{-5}, 10^{-4}, 10^{-3}\}$, $R_u \in \{0.5, 0.75, 1\}$, and the times indicated in the legends.

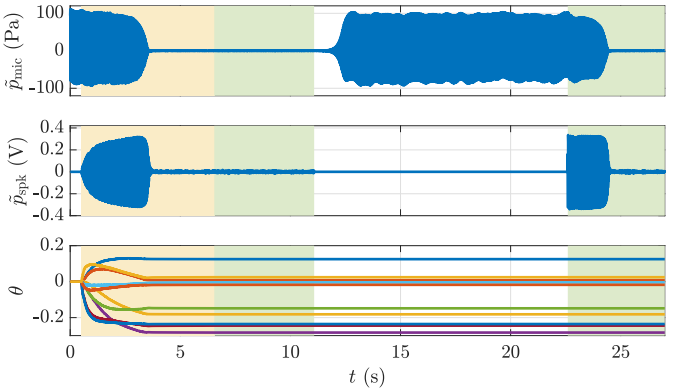

Fig. 25. Performance evaluation of the frozen-gain adaptive controller. Results from the closed-loop experiment using the frozen-gain adaptive controller. The pressure measurements $\tilde{p}_{\text{mic}}$, requested speaker voltage $\tilde{p}_{\text{spk}}$, and controller coefficients θ are shown. The white, yellow, and green shading corresponds to Modes 1–3, respectively.

D. Rijke-Tube Time-Varying Parameter Experiments

We now consider experimental scenarios where the experimental Rijke-tube setup is modified during closed-loop operation. In particular, the coil position and Variac voltage are changed during the experiments. The following procedure consists of seven phases as follows.

1) *Phase 1:* The experiment begins in Mode 1.
2) *Phase 2:* The experiment transitions to Mode 2 after the oscillations are formed.
3) *Phase 3:* After no further oscillation suppression is achieved, the experiment transitions to Mode 3.
4) *Phase 4:* Either the coil position is decreased or the Variac voltage is increased.

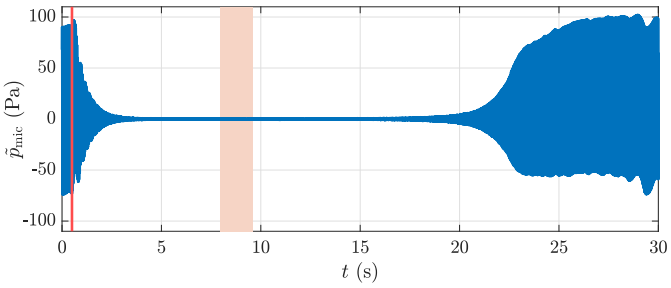

Fig. 26. Rijke-tube time-varying parameter experiments. Pressure measurements $\tilde{p}_{\text{mic}}$ from a closed-loop experiment using the constant-gain proportional controller in Fig. 14 are shown for $K = 0.05$. In this experiment, the coil voltage transitions from $V_{\text{rms}} = 70$ V to $V_{\text{rms}} = 90$ V with the coil position maintained at $x_{\text{us}} = 0.3$ m. The constant-gain proportional controller is initially disabled and is enabled at the time indicated by the red vertical line. The red shading denotes the time interval during which the coil voltage transitions from $V_{\text{rms}} = 70$ V to $V_{\text{rms}} = 90$ V.

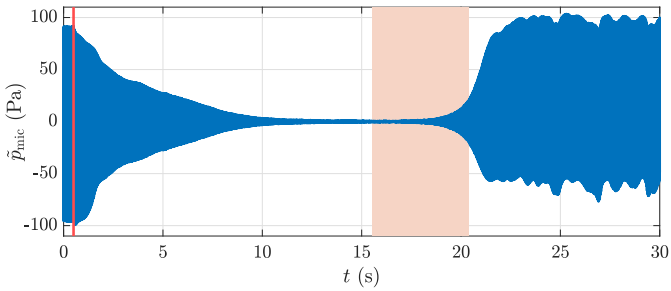

Fig. 27. Rijke-tube time-varying parameter experiments. Pressure measurements $\tilde{p}_{\text{mic}}$ from a closed-loop experiment using the constant-gain proportional controller in Fig. 14 are shown for $K = 0.05$. In this experiment, the coil position transitions from $x_{\text{us}} = 0.4$ m to $x_{\text{us}} = 0.3$ m with the coil voltage maintained at $V_{\text{rms}} = 90$ V. The constant-gain proportional controller is initially disabled and is enabled at the time indicated by the red vertical line. The red shading denotes the time interval during which the coil location transitions from $x_{\text{us}} = 0.4$ m to $x_{\text{us}} = 0.3$ m.

5) *Phase 5:* After some time, the experiment transitions to Mode 1, which allows oscillations to recover their open-loop amplitude.
6) *Phase 6:* The experiment transitions to Mode 3 (frozen-gain adaptive controller is implemented) after the oscillations recover their open-loop amplitude.
7) *Phase 7:* After approximately 30 s, the experiment transitions to Mode 2.

For the experiment where the coil voltage is changed, the voltage is changed from $V_{\text{rms}} = 70$ V to $V_{\text{rms}} = 90$ V with the coil position maintained at $x_{\text{us}} = 0.3$ m. For the experiment where the coil position is changed, the position is changed from $x_{\text{us}} = 0.4$ m to $x_{\text{us}} = 0.3$ m with the coil voltage maintained at $V_{\text{rms}} = 90$ V. Fig. 5 shows that the magnitudes of the peaks of the amplitude spectra increase after each transition.

For comparison, the constant-gain proportional controller introduced in Section VIII-A and shown in Fig. 14 with $K = 0.05$ is implemented in the same experimental scenarios. The results are shown in Figs. 26 and 27. In both experimental scenarios, the oscillation suppression achieved by the constant-gain proportional controller before either the coil position or the Variac voltage is changed is at least 38.69 dB. After either the coil position or the Variac voltage is changed, the oscillations recover their open-loop amplitude, and the constant-gain proportional controller yields no suppression.

For the adaptive suppression experiments, $l_{\text{c}} = 5$, $p_0 = 10^{-4}$, $R_u = 0.75$, and $G_{\text{f}}(\mathbf{q}) = -1/\mathbf{q}$ are used, as in Section VIII-C. The adaptive controller suppression results are shown in Figs. 28–31. At the end of Phase 2, the oscillation suppression achieved by the adaptive controller is at least 43.83 dB in both experimental scenarios. Throughout Phases 3 and 4, the frozen-gain adaptive controller maintains the oscillation suppression obtained at the end of the previous phase. At the end of Phase 6, the oscillation suppression achieved by the frozen-gain adaptive controller is at least 1.73 dB. At the end of Phase 7, the oscillation suppression achieved by the adaptive controller is at least 51.91 dB. Hence, after Phase 6, further adaptation suppresses the oscillations. Furthermore, Figs. 29 and 31 show that, in both scenarios, the peak of the magnitude response of the adaptive controller near $\pi/4$ rad/sample at the end of Phase 3 subsequently increases in magnitude during Phase 7.

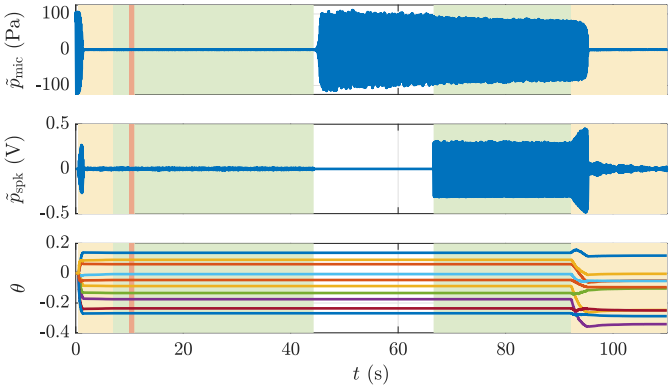

Fig. 28. Rijke-tube time-varying parameter experiments. Results from the closed-loop experiment using the adaptive controller where the coil voltage transitions from $V_{\text{rms}} = 70$ V to $V_{\text{rms}} = 90$ V with the coil position maintained at $x_{\text{us}} = 0.3$ m. The pressure measurements $\tilde{p}_{\text{mic}}$, requested speaker voltage $\tilde{p}_{\text{spk}}$, and controller coefficients θ are shown. The white, yellow, and green shading corresponds to Modes 1–3, respectively. The red shading denotes the time interval during which the coil voltage transitions from $V_{\text{rms}} = 70$ V to $V_{\text{rms}} = 90$ V.

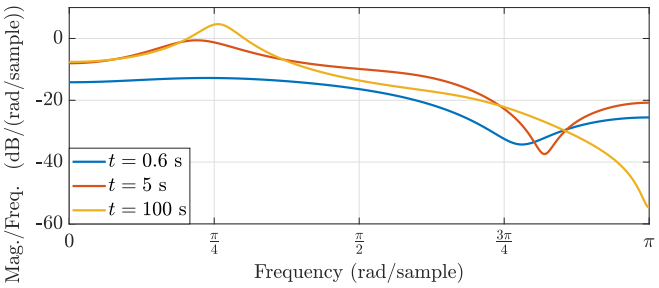

Fig. 29. Rijke-tube time-varying parameter experiments. The magnitude response of the adaptive controller for the closed-loop experiment where the coil voltage transitions from $V_{\text{rms}} = 70$ V to $V_{\text{rms}} = 90$ V with the coil position maintained at $x_{\text{us}} = 0.3$ m is shown for $t \in \{0.6, 5, 100\}$ s.

E. Gain-Margin Experiments

We now consider experimental scenarios where the gain of the adaptive controller is modified. These scenarios are

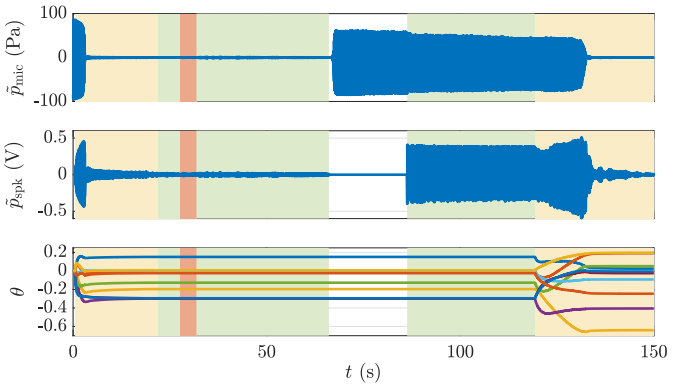

Fig. 30. Rijke-tube time-varying parameter experiments. Results from the closed-loop experiment using the adaptive controller where the coil position transitions from $x_{\text{us}} = 0.4$ m to $x_{\text{us}} = 0.3$ m with the coil voltage maintained at $V_{\text{rms}} = 90$ V. The pressure measurements $\tilde{p}_{\text{mic}}$, requested speaker voltage $\tilde{p}_{\text{spk}}$, and controller coefficients θ are shown. The white, yellow, and green shading corresponds to Modes 1–3, respectively. The red shading denotes the time interval during which the coil location transitions from $x_{\text{us}} = 0.4$ m to $x_{\text{us}} = 0.3$ m.

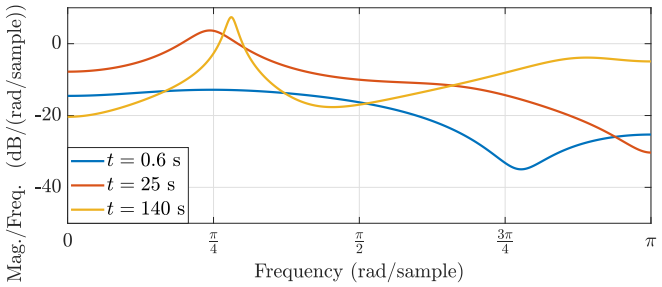

Fig. 31. Rijke-tube time-varying parameter experiments. The magnitude response of the adaptive controller for the closed-loop experiment where the coil position transitions from $x_{\text{us}} = 0.4$ m to $x_{\text{us}} = 0.3$ m with the coil voltage maintained at $V_{\text{rms}} = 90$ V is shown for $t \in \{0.6, 25, 140\}$ s.

conducted for $x_{\text{us}} = 0.3$ m and $V_{\text{rms}} = 90$ V. The controller output is multiplied by α, as shown in Fig. 32, which is initially set to $\alpha = 1$. Each scenario begins in Mode 1 and transitions to Mode 2 after the oscillations are formed. After no further oscillation suppression is achieved, two experimental scenarios are considered.

1) *Scenario 1:* The experiment continues to operate in Mode 2.
2) *Scenario 2:* The experiment transitions to Mode 3.

After this, in each scenario, the value of α is changed when no further suppression is achieved. For these experiments, $l_{\text{c}} = 5$, $p_0 = 10^{-4}$, $R_u = 0.75$, and $G_{\text{f}}(\mathbf{q}) = -1/\mathbf{q}$ are used, as shown in Section VIII-C.

Experimental results are shown in Fig. 33. In Scenario 1, increases in α yield a slight decrease in oscillation suppression, while decreases in α yield oscillation suppression similar to the case where $\alpha = 1$. In Scenario 2, increases in α yield a slight decrease in oscillation suppression, while decreases in α yield a noticeable decrease in oscillation suppression. Hence, the adaptive controller maintains oscillation suppression under changes in its gain.

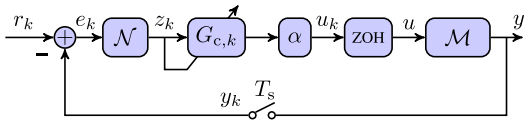

Fig. 32. Adaptive control of $\mathcal{M}$ with controller gain α.

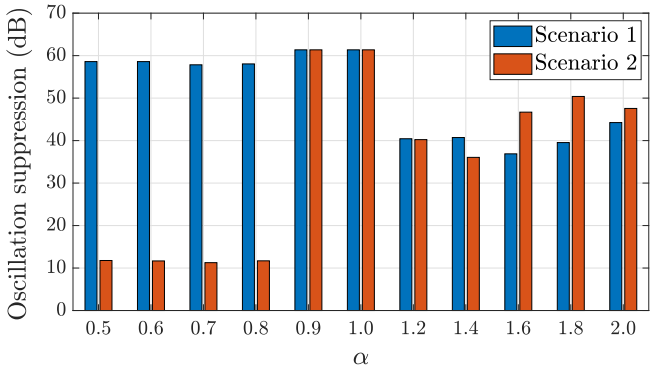

Fig. 33. Gain-margin tests. Oscillation suppression using the controller architecture in Fig. 32 is shown for varying values of α. After no further oscillation suppression is achieved in the case where $\alpha = 1$, two experimental scenarios are considered. In Scenario 1, the experiment continues to operate in Mode 2. In Scenario 2, the experiment transitions to Mode 3. After this, in each scenario, the value of α is changed when no further suppression is achieved.

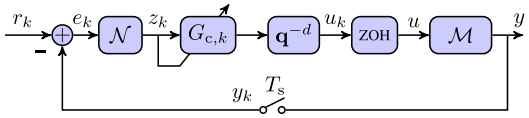

Fig. 34. Adaptive control of $\mathcal{M}$ with controller delay of d steps.

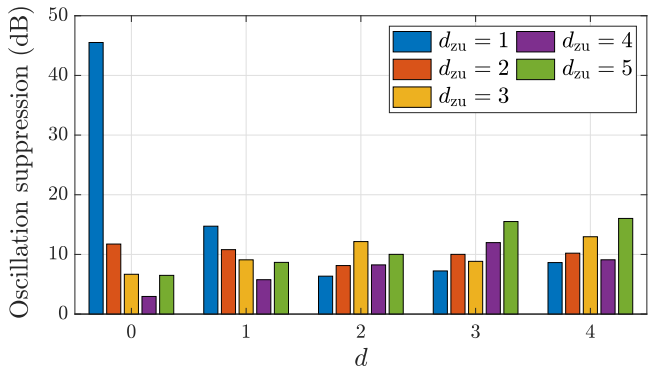

Fig. 35. G_{f} relative-degree experiments. G_{f} relative-degree experimental results using the controller architecture in Fig. 34 are shown for various values of the input delay d and the relative degree d_{zu} of G_{f}.

F. G_{f} Relative-Degree Experiments

We now consider experimental scenarios involving input delay and changes in the relative degree of G_{f}. These experiments are conducted for $x_{\text{us}} = 0.3$ m and $V_{\text{rms}} = 90$ V. For these experiments, an input delay of d steps is added to the control architecture, as shown in Fig. 34. The experiment begins in Mode 1 and transitions to Mode 2 after the oscillations are formed. Afterward, the experiment continues to operate in Mode 2. For this test, the hyperparameters are given by $l_{\text{c}} = 5$, $p_0 = 10^{-4}$, and $R_u = 0.75$, as in

Section VIII-C. Furthermore, $G_{\mathrm{f}}(\mathbf{q}) = -\mathbf{q}^{-d_{\mathrm{zu}}}$, where d_{zu} determines the relative degree of G_{f}. Note that $d_{\mathrm{zu}} = 1$ in Sections VIII-A–VIII-E.

The experimental results are shown in Fig. 35. For all $d \in \{0, 1, 2, 3, 4\}$, the values of d_{zu} that yield the greatest oscillation suppression lie within $\{d-1, d, d+1\}$.

IX. Conclusion

This article described an experimental Rijke-tube setup and its open-loop response under various system parameters. For adaptive control, a hyperparameter selection procedure was proposed. This procedure consists of tuning a Rijke-tube model to emulate the first modal peak of the open-loop response of the experimental Rijke-tube setup under a single choice of system parameters, applying the adaptive controller to the emulation model, and running numerical simulations to determine hyperparameters that suppress the model oscillations. The selected hyperparameters were then used by the adaptive controller to suppress the oscillatory response of the experimental Rijke-tube setup under various system parameters. Further experiments showed the effect of modified hyperparameters on the time it takes for the adaptive controller to suppress oscillations, the performance and robustness of the frozen-gain adaptive controller, the ability of the adaptive controller to readapt under changes in working conditions, the stability of the adaptive controller under changes in its gain, and the effect of the relative degree of the closed-loop target model on the level of suppression.

Acknowledgment

The authors thank Aseem Islam for helpful discussions, John Spencer for assistance with the experiments, Karl Grosh for help on acoustics, and the reviewers for numerous suggestions.

References

[1] J. P. Epperlein, B. Bamieh, and K. J. Astrom, "Thermoacoustics and the Rijke tube: Experiments, identification, and modeling," *IEEE Contr. Sys. Mag.*, vol. 35, no. 2, pp. 57–77, Apr. 2015.

[2] B. Chance, E. K. Pye, A. K. Ghosh, and B. Hess, Eds., *Biological and Biochemical Oscillators*. New York, NY, USA: Academic, 1973.

[3] P. Gray and S. K. Scott, *Chemical Oscillations and Instabilities: Non-Linear Chemical Kinetics*. Oxford, U.K.: Clarendon, 1990.

[4] A. Goldbeter and M. J. Berridge, *Biochemical Oscillations and Cellular Rhythms: The Molecular Bases of Periodic and Chaotic Behaviour*. Cambridge, U.K.: Cambridge Univ. Press, 1996.

[5] Y. Chen and J. F. Driscoll, "A multi-chamber model of combustion instabilities and its assessment using kilohertz laser diagnostics in a gas turbine model combustor," *Combustion Flame*, vol. 174, pp. 120–137, Dec. 2016.

[6] E. Awad and F. E. C. Culick, "On the existence and stability of limit cycles.For longitudinal acoustic modes in a combustion chamber," *Combustion Sci. Technol.*, vol. 46, nos. 3–6, pp. 195–222, Apr. 1986.

[7] A. Jenkins, "Self-oscillation," *Phys. Rep.*, vol. 525, no. 2, pp. 167–222, 2013.

[8] W. Ding, *Self-Excited Vibration: Theory, Paradigms, and Research Methods*. Cham, Switzerland: Springer, 2010.

[9] E. Jonsson, C. Riso, C. A. Lupp, C. E. S. Cesnik, J. R. R. A. Martins, and B. I. Epureanu, "Flutter and post-flutter constraints in aircraft design optimization," *Prog. Aerosp. Sci.*, vol. 109, Aug. 2019, Art. no. 100537.

[10] B. D. Coller and P. A. Chamara, "Structural non-linearities and the nature of the classic flutter instability," *J. Sound Vibrat.*, vol. 277, nos. 4–5, pp. 711–739, Nov. 2004.

[11] P. P. Friedmann, "Renaissance of aeroelasticity and its future," *J. Aircr.*, vol. 36, no. 1, pp. 105–121, Jan. 1999.

[12] D. Green and W. G. Unruh, "The failure of the Tacoma bridge: A physical model," *Amer. J. Phys.*, vol. 74, no. 8, pp. 706–716, Aug. 2006.

[13] A. P. Dowling and A. S. Morgans, "Feedback control of combustion oscillations," *Annu. Rev. Fluid Mech.*, vol. 37, pp. 151–182, Jan. 2005.

[14] T. Yi and E. J. Gutmark, "Adaptive control of combustion instability based on dominant acoustic modes reconstruction," *Combustion Sci. Technol.*, vol. 180, no. 2, pp. 249–263, Dec. 2007.

[15] A. Banaszuk, Y. Zhang, and C. A. Jacobson, "Adaptive control of combustion instability using extremum-seeking," in *Proc. Amer. Control Conf. (ACC)*, Jun. 2000, pp. 416–422.

[16] S. Evesque and A. Dowling, "Adaptive control of combustion oscillations," in *Proc. 4th AIAA/CEAS Aeroacoustics Conf.*, Jun. 1998, p. 2351.

[17] S. Koshigoe, T. Komatsuzaki, and V. Yang, "Adaptive control of combustion instability with on-line system identification," *J. Propuls. Power*, vol. 15, no. 3, pp. 383–389, May 1999.

[18] G. Billoud, M. A. Galland, C. H. Huu, and E. S. Cancel, "Adaptive active control of combustion instabilities," *Combustion Sci. Technol.*, vol. 81, nos. 4–6, pp. 257–283, Feb. 1992.

[19] P. L. Rijke, "LXXI. Notice of a new method of causing a vibration of the air contained in a tube open at both ends," *London, Edinburgh, Dublin Phil. Mag. J. Sci.*, vol. 17, no. 116, pp. 419–422, Jun. 1859.

[20] W. S. Rayleigh, "The explanation of certain acoustical phenomena," *Nature*, vol. 18, no. 455, pp. 319–321, 1878.

[21] A. P. Dowling, "The calculation of thermoacoustic oscillations," *J. Sound Vibrat.*, vol. 180, no. 4, pp. 557–581, Mar. 1995.

[22] J. J. Keller, "Thermoacoustic oscillations in combustion chambers of gas turbines," *AIAA J.*, vol. 33, no. 12, pp. 2280–2287, Dec. 1995.

[23] L. Kabiraj and R. Sujith, "Nonlinear self-excited thermoacoustic oscillations: Intermittency and flame blowout," *J. Fluid Mech.*, vol. 713, nos. 376–397, p. 13, 2012.

[24] T. C. Lieuwen and V. Yang, *Combustion Instabilities in Gas Turbine Engines: Operational Experience, Fundamental Mechanisms, and Modeling*. Reston, VA, USA: AIAA, 2005.

[25] M. A. Heckl, "Non-linear acoustic effects in the Rijke tube," *Acta Acustica*, vol. 72, no. 1, pp. 63–71, 1990.

[26] S. Bittanti, A. De Marco, G. Poncia, and W. Prandoni, "Identification of a model for thermoacoustic instabilities in a Rijke tube," *IEEE Trans. Control Syst. Technol.*, vol. 10, no. 4, pp. 490–502, Jul. 2002.

[27] K. I. Matveev, "Energy consideration of the nonlinear effects in a Rijke tube," *J. Fluids Struct.*, vol. 18, no. 6, pp. 783–794, Dec. 2003.

[28] K. Balasubramanian and R. I. Sujith, "Thermoacoustic instability in a Rijke tube: Non-normality and nonlinearity," *Phys. Fluids*, vol. 20, no. 4, Apr. 2008, Art. no. 044103.

[29] N. Olgac, U. Zalluhoglu, and A. S. Kammer, "Predicting thermoacoustic instability: A novel analytical approach and its experimental validation," *J. Propuls. Power*, vol. 30, no. 4, pp. 1005–1015, 2014.

[30] J. Rubio-Hervas, M. Reyhanoglu, and W. MacKunis, "Observer-based sliding mode control of rijke-type combustion instability," *J. Low Freq. Noise, Vibrat. Act. Control*, vol. 34, no. 2, pp. 201–217, Jun. 2015.

[31] G. A. de Andrade, R. Vazquez, and D. J. Pagano, "Backstepping-based estimation of thermoacoustic oscillations in a Rijke tube with experimental validation," *IEEE Trans. Autom. Control*, vol. 65, no. 12, pp. 5336–5343, Dec. 2020.

[32] A. M. Annaswamy and A. F. Ghoniem, "Active control of combustion instability: Theory and practice," *IEEE Control Syst.*, vol. 22, no. 6, pp. 37–54, Dec. 2002.

[33] Y. Huang and V. Yang, "Dynamics and stability of lean-premixed swirl-stabilized combustion," *Prog. Energy Combustion Sci.*, vol. 35, no. 4, pp. 293–364, 2009.

[34] M. A. Heckl, "Active control of the noise from a Rijke tube," *J. Sound Vib.*, vol. 124, no. 1, pp. 117–133, 1988.

[35] U. Zalluhoglu, A. S. Kammer, and N. Olgac, "Delayed feedback control laws for Rijke tube thermoacoustic instability, synthesis, and experimental validation," *IEEE Trans. Control Syst. Technol.*, vol. 24, no. 5, pp. 1861–1868, Sep. 2016.

[36] G. A. de Andrade, R. Vazquez, and D. J. Pagano, "Boundary control of a Rijke tube using irrational transfer functions with experimental validation," in *Proc. IFAC World Congress*, 2017, pp. 4528–4533.

[37] A. Kemal and C. T. Bowman, "Real-time adaptive feedback control of combustion instability," in *Proc. Int. Symp. Combustion*, 1996, pp. 2803–2809.

[38] A. M. Annaswamy, M. Fleifil, J. W. Rumsey, R. Prasanth, J.-P. Hathout, and A. F. Ghoniem, "Thermoacoustic instability: Model-based optimal control designs and experimental validation," *IEEE Trans. Control Syst. Technol.*, vol. 8, no. 6, pp. 905–918, Nov. 2000.

[39] A. S. Morgans and A. M. Annaswamy, "Adaptive control of combustion instabilities for combustion systems with right-half plane zeros," *Combustion Sci. Technol.*, vol. 180, no. 9, pp. 1549–1571, Jul. 2008.

[40] M. A. Vaudrey, W. T. Baumann, and W. R. Saunders, "Time-averaged gradient control of thermoacoustic instabilities," *J. Propuls. Power*, vol. 19, no. 5, pp. 830–836, Sep. 2003.

[41] S. Illingworth and A. Morgans, "Advances in feedback control of the Rijke tube thermoacoustic instability," *Int. J. Flow Control*, vol. 2, no. 4, pp. 197–218, Dec. 2010.

[42] W. Wei, J. Wang, D.-H. Li, M. Zhu, H.-J. Tang, and F.-L. Weng, "Dynamic compensation based adaptive control of thermo-acoustic instabilities in Rijke tube: An experimental validation," *ISA Trans.*, vol. 52, no. 3, pp. 450–460, May 2013.

[43] R. Blonbou, A. Laverdant, S. Zaleski, and P. Kuentzmann, "Active control of combustion instabilities on a Rijke tube using neural networks," *Proc. Combustion Inst.*, vol. 28, no. 1, pp. 747–755, Jan. 2000.

[44] G. A. de Andrade, R. Vazquez, and D. J. Pagano, "Backstepping stabilization of a linearized ODE–PDE Rijke tube model," *Automatica*, vol. 96, pp. 98–109, Oct. 2018.

[45] Y. Rahman, A. Xie, and D. S. Bernstein, "Retrospective cost adaptive control: Pole placement, frequency response, and connections with LQG control," *IEEE Control Syst.*, vol. 37, no. 5, pp. 28–69, Oct. 2017.

[46] S. A. U. Islam, T. W. Nguyen, I. V. Kolmanovsky, and D. S. Bernstein, "Data-driven retrospective cost adaptive control for flight control applications," *J. Guid., Control, Dyn.*, vol. 44, no. 10, pp. 1732–1758, Oct. 2021.

[47] J. B. Hoagg and D. S. Bernstein, "Retrospective cost model reference adaptive control for nonminimum-phase systems," *J. Guid., Control, Dyn.*, vol. 35, no. 6, pp. 1767–1786, Nov. 2012.

[48] J. Paredes, S. A. U. Islam, and D. S. Bernstein, "Adaptive stabilization of thermoacoustic oscillations in a Rijke tube," in *Proc. Amer. Contr. Conf.*, 2022, pp. 28–33.

[49] E. D. Sumer and D. Bernstein, "Retrospective cost adaptive control with error-dependent regularization for MIMO systems with uncertain nonminimum-phase transmission zeros," in *Proc. AIAA Guid., Navigat., Control Conf.*, Aug. 2012, pp. 1–19.

[50] L. Ljung and T. Soderstrom, *Theory and Practice of Recursive Identification*. Cambridge, MA, USA: MIT Press, 1983.

[51] S. A. U. Islam and D. S. Bernstein, "Recursive least squares for real-time implementation [lecture notes]," *IEEE Control Syst.*, vol. 39, no. 3, pp. 82–85, Jun. 2019.

[52] S. M. Sarpotdar, N. Ananthkrishnan, and S. D. Sharma, "The Rijke tube—A thermo-acoustic device," *Resonance*, vol. 8, no. 1, pp. 59–71, Jan. 2003.

[53] R. L. Raun, M. W. Beckstead, J. C. Finlinson, and K. P. Brooks, "A review of Rijke tubes, Rijke burners and related devices," *Prog. Energy Combustion Sci.*, vol. 19, no. 4, pp. 313–364, Jan. 1993.

[54] K. Manoj, S. A. Pawar, J. Kurths, and R. I. Sujith, "Rijke tube: A nonlinear oscillator," *Chaos, Interdiscipl. J. Nonlinear Sci.*, vol. 32, no. 7, Jul. 2022, Art. no. 072101.

[55] J. W. S. Rayleigh, *The Theory of Sound*, vol. 2. New York, NY, USA: Macmillan & Company, 1896.

[56] A. P. Dowling, "Nonlinear self-excited oscillations of a ducted flame," *J. Fluid Mech.*, vol. 346, pp. 271–291, Sep. 1997.

[57] B. A. Francis and W. M. Wonham, "The internal model principle of control theory," *Automatica*, vol. 12, no. 5, pp. 457–465, 1976.